


## PAPER



Cite this: *Dalton Trans.*, 2021, **50**, 2375

# Surface peptide functionalization of zeolitic imidazolate framework-8 for autonomous homing and enhanced delivery of chemotherapeutic agent to lung tumor cells†

Nurul Akmarina Mohd Abdul Kamal,<sup>a,b,c</sup> Emilia Abdulmalek,<sup>a</sup> Sharida Fakurazi,<sup>d</sup> Kyle E. Cordova <sup>\*e</sup> and Mohd Basyaruddin Abdul Rahman<sup>\*a,b</sup>

Chemotherapeutic agents used in treating certain cancer types operate in a non-selective manner tending to accumulate in normal, healthy tissue when high doses are used. To mitigate the toxicity effect resulting from this, there is an urgent need to develop active nano delivery systems capable of regulating optimal doses specifically to cancer cells without harming adjacent normal cells. Herein, we report a versatile nanoparticle – zeolitic imidazolate framework-8 (nZIF-8) – that is loaded with a chemotherapeutic agent (gemcitabine; GEM) and surface-functionalized with an autonomous homing system (Arg-Gly-Asp peptide ligand; RGD) via a straightforward, one-pot solvothermal reaction. Successful functionalization of the surface of nZIF-8 loaded GEM (GEMcnZIF-8) with RGD was proven by spectroscopic and electron microscopy techniques. This surface-functionalized nanoparticle (GEMcRGD@nZIF-8) exhibited enhanced uptake in human lung cancer cells (A549), compared with non-functionalized GEMcnZIF-8. The GEMcRGD@nZIF-8, experienced not only efficient uptake within A549, but also induced obvious cytotoxicity (75% at a concentration of 10  $\mu\text{g mL}^{-1}$ ) and apoptosis (62%) after 48 h treatment when compared to the nanoparticle absent of the RGD homing system (GEMcnZIF-8). Most importantly, this surface-functionalized nanoparticle was more selective towards lung cancer cells (A549) than normal human lung fibroblast cells (MRC-5) with a selectivity index (SI) of 3.98. This work demonstrates a new one-pot strategy for realizing a surface-functionalized zeolitic imidazolate framework that actively targets cancer cells via an autonomous homing peptide system to deliver a chemotherapeutic payload effectively.

Received 13th January 2021,  
Accepted 2nd February 2021

DOI: 10.1039/d1dt00116g

rsc.li/dalton

## Introduction

Lung cancer has one of the highest prevalence rates with the poorest prognoses amongst cancer types.<sup>1</sup> Over 50% of those

diagnosed with lung cancer die within their first year of diagnosis, beyond which time, less than 18% will survive after the fifth year.<sup>2</sup> Traditionally, the primary approach for treating lung cancer remains chemotherapy, in which gemcitabine (GEM) is employed alone or in combination with other chemotherapeutic agents.<sup>3–5</sup> As is similar with other chemotherapeutic agents, GEM functions in a non-selective manner and tends to accumulate in healthy tissue with high doses; two properties that lead to severe toxicity of normal cells.<sup>6,7</sup> As such, there exists an urgent need to rectify this situation by developing targeted chemotherapeutic delivery systems that are capable of regulating optimal doses specifically to cancer cells without harming adjacent and ever-present normal, healthy cells.<sup>8–11</sup>

To realize such systems, research attention has been placed on the creation and use of nanocarriers.<sup>12</sup> Different types of nanocarriers have been formulated with varying degrees of success.<sup>13</sup> Indeed, several classes have exhibited excellent performance in clinical phase trials.<sup>14,15</sup> As a representative

<sup>a</sup>Integrated Chemical BioPhysics Research, Department of Chemistry, Faculty of Science, Universiti Putra Malaysia (UPM), Serdang 43400, Selangor, Malaysia.

E-mail: basya@upm.edu.my

<sup>b</sup>UPM-MAKNA Cancer Laboratory, Institute of Bioscience, UPM, Serdang 43400, Selangor, Malaysia

<sup>c</sup>Faculty of Chemical and Process Engineering Technology, Universiti Malaysia Pahang (UMP), Pekan 26600, Pahang, Malaysia

<sup>d</sup>Department of Human Anatomy, Faculty of Medicine and Health Sciences, UPM, Serdang 43400, Selangor, Malaysia

<sup>e</sup>Materials Discovery Research Unit, Advanced Research Centre, Royal Scientific Society, Amman 11941, Jordan. E-mail: kyle.cordova@rss.jo

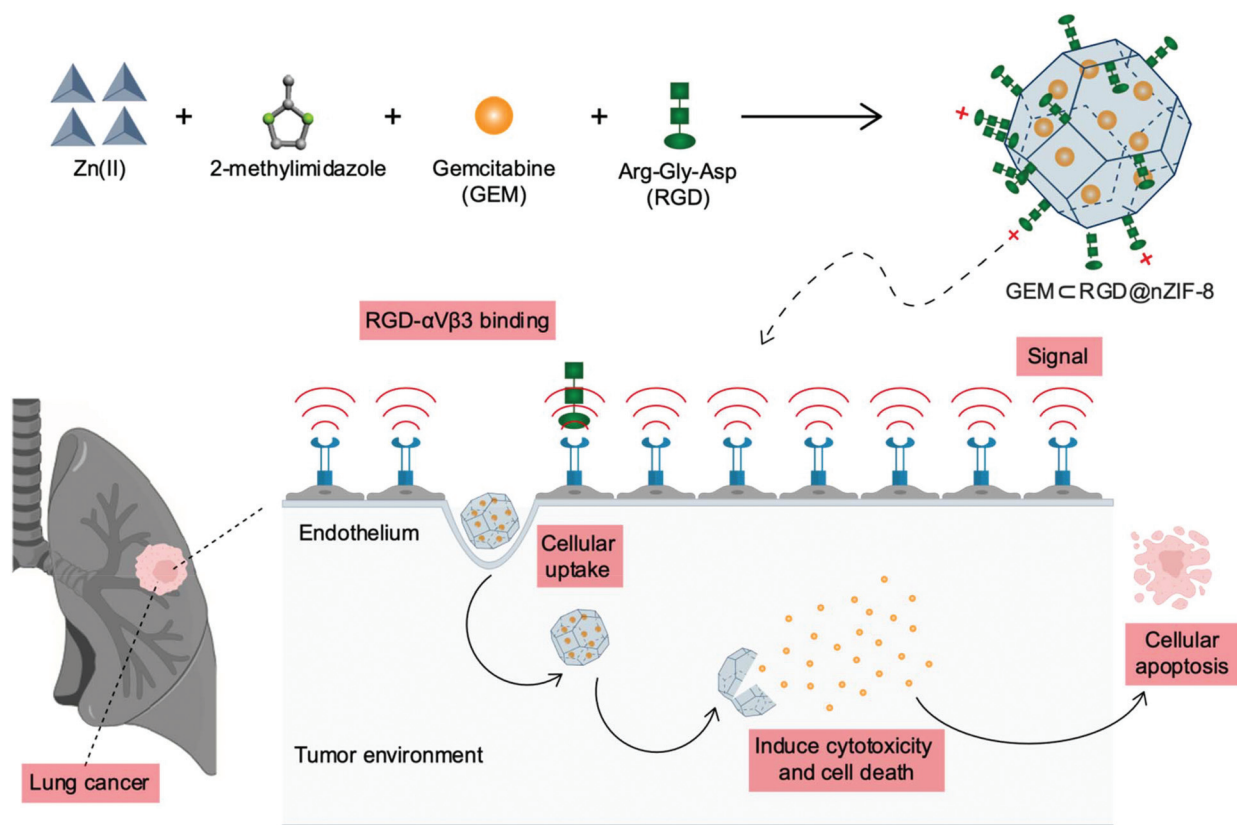
†Electronic supplementary information (ESI) available: Fig. S1–S6. Additional characterization, including, but not limited to, N<sub>2</sub> isotherms, thermal gravimetric analyses, size exclusion chromatography, HR-TEM images, AFM images and zeta potential. See DOI: 10.1039/d1dt00116g

example, nano-scale polymeric micelles have been clinically approved as a result of their ability to improve the low solubilities of hydrophobic chemotherapeutic agents.<sup>16</sup> Others based on lipids have also successfully improved the loading capacity of both hydrophobic and hydrophilic chemotherapeutic agents.<sup>17–19</sup> The general mechanism by which these nanocarriers operate is most often one of a passive-targeting strategy, whereby the nanocarriers take advantage of tumor-pathophysiological conditions, including tumor vascularity and inadequate lymphatic drainage.<sup>20</sup> However, this mechanism is incapable of mitigating the toxicity effect of normal cells due to a lack of selectivity in where they off-load their therapeutic payload, which, often times, yields unpredictable accumulation in healthy tissue.

To advance the effectiveness of chemotherapeutic nanocarriers, it is essential to focus on developing such systems based on active-targeting mechanisms.<sup>21,22</sup> The most straightforward method for achieving this is to functionalize the surface of the nanocarrier with active ligands that specifically target certain cancer cells; examples of which include antibodies and peptides.<sup>23</sup> In general, peptides are deemed increasingly promising as certain sequences (*i.e.* Arg-Gly-Asp; RGD) are capable of selectively interacting with specific integ-

rin receptors ( $\alpha V\beta 3$ ) present on the tumor endothelia.<sup>24</sup> The general mechanism of such an interaction is akin to a 'homing device', whereby the RGD-functionalized nanocarrier navigates to a cancer cell, docks as a result of selective interactions with the specific integrin receptors, and delivers the chemotherapeutic agent.<sup>25,26</sup>

Herein, we report the synthesis and use of a nanoparticle, zeolitic imidazolate framework-8 (nZIF-8), as a nanocarrier that is loaded with GEM and surface-functionalized with the RGD homing peptide ligand to actively-target and specifically-deliver the chemotherapeutic agent to lung cancer cells (Scheme 1). The reasons for pursuing nZIF-8 as a nanocarrier is the fact that it is well-known to embody high porosity with large surface areas, possess adjustable particle sizes (nano- to millimeter scales), and often enjoy inherent biocompatibility.<sup>27–29</sup> Despite the fact that nZIF-8 in and of itself has no active-targeting properties, previous studies have shown that the surface of nZIF-8 can be modified through different reaction avenues and therapeutic agents can be efficiently loaded within and released from its pores.<sup>30–34</sup> After demonstrating the successful realization of this nanocarrier system, we demonstrated its effectiveness in actively transporting and delivering GEM to cancer cells.



**Scheme 1** Synthetic scheme for realizing the nanoparticle, GEM@RGD@nZIF-8, that actively targets cancer cells *via* an autonomous homing peptide system (RGD) on its surface in order to effectively deliver a chemotherapeutic agent (GEM). Once GEM@RGD@nZIF-8 has reached the tumoral endothelium surface, cellular uptake occurs and the chemotherapeutic agent induces cytotoxicity, cell death, and, ultimately, cellular apoptosis.

## Results and discussion

### Strategy for realizing autonomous homing nanoparticles

In our quest to realize a nanoparticle for the active and autonomous targeting of cancer cells for delivery of a chemotherapeutic payload, we sought two requisite structural features: (i) high porosity, which affords the ability to load optimal doses of anti-tumor agents; and (ii) surface customizability so as to ensure the active-targeting of cancer cells by the nanoparticle. To satisfy both structural requirements, we decided to pursue so-called reticular materials that are governed by reticular chemistry.<sup>35,36</sup> Zeolitic imidazolate frameworks (ZIFs), are a subclass of reticular materials, known for their high porosity, well-defined structures due to their crystallinity, and structural diversity.<sup>37</sup> ZIFs have been demonstrated capable of loading optimal quantities of chemotherapeutic agents within their pores, their surfaces have proven modifiable by a wide range of moieties, and their biocompatibility has been established.<sup>38</sup> Accordingly, ZIF-8, an archetypal reticular material adopting a sodalite structure, was chosen given its ease of synthesis on the nanoscale as well as the ease in which surface functionalization can be performed. To ensure that nano-ZIF-8 (nZIF-8) was capable of actively and autonomously targeting tumor cells, we chose to functionalize its surface with the Arg-Gly-Asp homing peptide ligand (RGD). The RGD peptide is a binding ligand that homes the integrin receptors  $\alpha V\beta 3$ , which are over-expressed on tumoral endothelia.<sup>39–42</sup> In the case that the RGD-functionalized nZIF-8 is carrying a chemotherapeutic payload, the reticular nanoparticle can dock on the surface of the cell to deliver the agents that are being carried. As a proof-of-concept, we synthesized and fully characterized nZIF-8, loaded it with the chemotherapeutic agent, gemcitabine (GEM), functionalized the surface of the nZIF-8 with the RGD peptide, and assessed the ability of this nanoparticle to induce apoptosis of tumor cells as a result of the actively and selectively delivered GEM.

### Synthesis, structural characterization, encapsulation efficiency and loading amount

The optimized synthetic recipes for realizing the reticular nanoparticles (nZIF-8), the chemotherapeutic agent loaded reticular nanoparticles (GEMCnZIF-8), and the loaded reticular nanoparticles whose surfaces were functionalized with RGD homing peptide ligands (GEMCRGD@nZIF-8) were found to be essentially the same with the synthesis of all three nanoparticles following a straightforward, one-pot solvothermal reaction procedure. Once each nanoparticle was isolated, washed, solvent-exchanged, and activated, powder X-ray diffraction (PXRD) analysis was performed. As shown in Fig. 1, the experimental diffraction patterns for nZIF-8, GEMCnZIF-8, and GEMCRGD@nZIF-8 were observed to be coincident with the theoretical diffraction pattern simulated from the single crystal structure of ZIF-8. This PXRD analysis provided several critical findings: (i) loading of GEM within nZIF-8 did not disrupt the crystallinity of the ZIF-8 structure; (ii) the structure of nZIF-8 was robust enough to withstand the conditions

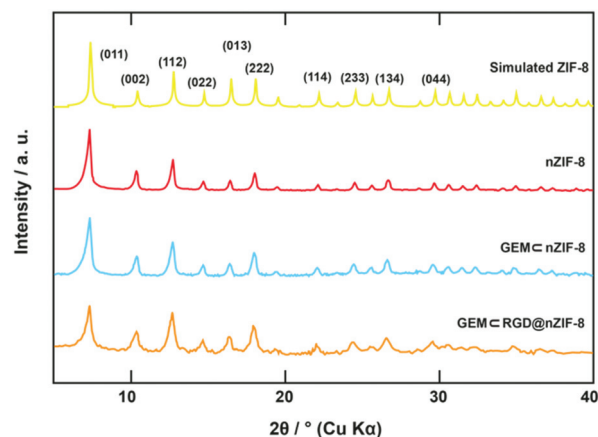


**Fig. 1** Powder X-ray diffraction (PXRD) patterns for nZIF-8 (red), GEMCnZIF-8 (blue), and GEMCRGD@nZIF-8 (orange). These experimental PXRD patterns are presented in comparison to the diffraction pattern simulated from the crystal structure of ZIF-8 (yellow).

needed to modify its surface with RGD; and (iii) bulk phase purity of all three nanoparticles was proven.

Prior to further structural characterization, the GEM loading amount and encapsulation efficiency was determined by reaction supernatant analysis *via* HPLC. Although both GEMCnZIF-8 and GEMCRGD@nZIF-8 achieved high encapsulation efficiencies of 96.9 and 97.3%, respectively, the loading amounts were determined to be relatively low (8.6 and 7.8%, respectively). The reason for this is two-fold: (i) loading is limited by the amount of GEM added during the synthesis (8 mg in 1 mL methanol); and (ii) low loading amounts are likely a consequence of the synthesis process, in which GEM is able to diffuse out of the nZIF-8 framework as it begins to crystallize. When comparing to values reported in the literature, both the encapsulation efficiency and loading amount are acceptable for achieving optimal therapeutic efficiency.<sup>43,44</sup> Permanent porosity and architectural robustness were proven by  $N_2$  isotherms at 77 K and thermal gravimetric analyses (TGA), respectively. As expected, the Brunauer–Emmett–Teller surface areas as calculated from the  $N_2$  isotherms, were found to decrease when comparing nZIF-8 ( $1550 \text{ m}^2 \text{ g}^{-1}$ ) with GEMCnZIF-8 ( $1535 \text{ m}^2 \text{ g}^{-1}$ ) and GEMCRGD@nZIF-8 ( $1480 \text{ m}^2 \text{ g}^{-1}$ ) (see ESI, Fig. S1†). At relatively low pressure ( $P/P_0 < 0.01$ ), the nitrogen adsorption increased steeply, highlighting the microporosity of the framework. The results were in line with those reported previously.<sup>45</sup> Similarly, TGA under  $N_2$  flow, depicts a trend of GEMCRGD@nZIF-8 < GEMCnZIF-8 < nZIF-8 with respect to thermal stability (see ESI, Fig. S2†). Both GEMCRGD@nZIF-8 and GEMCnZIF-8 begin to thermally decompose over the 370–450 °C range whereas nZIF-8 is thermally stable up to at least 530 °C.

### Characterization of the surface functionalization of GEMCnZIF-8 by RGD homing peptide ligands

Successful surface functionalization of GEMCnZIF-8 by RGD was first confirmed by Fourier transform infrared spectroscopy

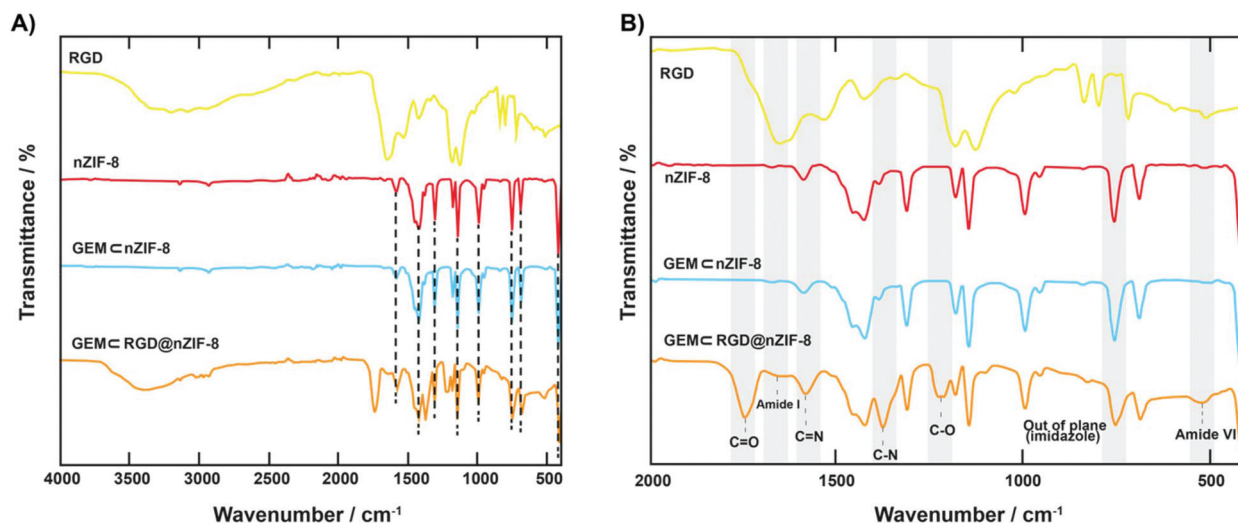


**Fig. 2** Fourier transform-infrared spectroscopy (FT-IR) spectra comparing nZIF-8 (red), GEMcnZIF-8 (blue), and GEMcRGD@nZIF-8 (orange) in comparison with the spectrum for the pristine RGD homing peptide ligand (yellow). (A) Full spectra of nanoparticles and (B) close-up on those absorption bands directly related to the identification of the successful surface functionalization of nZIF-8 with RGD are highlighted in light grey.

measurements (FT-IR) (Fig. 2). The parent nZIF-8 FT-IR spectrum exhibited a number of characteristic absorption bands that serve as a baseline for comparison with RGD surface functionalized nZIF-8: (i)  $1577\text{ cm}^{-1}$  and  $1450\text{--}1300\text{ cm}^{-1}$  correspond to  $\nu_{\text{C}=\text{N}}$  of 2-methylimidazolate and ring stretching frequencies, respectively; (ii)  $1142$  and  $992\text{ cm}^{-1}$  are attributed to  $\nu_{\text{C}-\text{N}}$  of 2-methylimidazolate stretching and bending, respectively; (iii)  $691\text{ cm}^{-1}$  is assigned to a 2-methylimidazolate ring out-of-plane bending frequency; and, finally, (iv)  $420\text{ cm}^{-1}$  can be ascribed to  $\nu_{\text{Zn}-\text{N}}$  stretching frequency, thereby, suggesting bond formation between tetrahedral  $\text{Zn}^{2+}$  and 2-methylimidazolate-derived N atoms (Fig. 2A). Indeed, these observed absorption bands are in agreement with those reported previously.<sup>45,46</sup> The close up FT-IR spectrum (Fig. 2B) upon functionalization of the surface of nZIF-8 with the RGD homing peptide shows considerable differences when compared with the parent nZIF-8 spectrum. It is important to first note that all those absorption bands observed in the FT-IR spectrum for the parent nZIF-8 remain present in the FT-IR spectrum for GEMcRGD@nZIF-8. Secondly, several characteristic absorption bands of RGD emerge as follows: (i)  $3300\text{--}3100\text{ cm}^{-1}$  corresponds to overlapping amide A and B absorption bands; (ii)  $1736\text{ cm}^{-1}$  strongly indicates the presence of a  $\nu_{\text{C}=\text{O}}$  stretching frequency that is characteristic of any given peptide; (iii)  $1648\text{ cm}^{-1}$  is assigned to amide I; (iv)  $1577\text{ cm}^{-1}$  exhibits a slight increase in absorbance due to an overlap of  $\nu_{\text{C}=\text{N}}$  between the 2-methylimidazolate of nZIF-8 and the Arg residue of RGD. We speculate that the Arginine residue of RGD acts as a Lewis base while interacting with coordinatively unsaturated Zn(II) sites at the surface of the nZIF-8 crystal;<sup>47</sup> (v)  $1375\text{ cm}^{-1}$  is ascribed to a  $\nu_{\text{C}-\text{N}}$  stretching frequency originating from RGD; and (vi)  $524\text{ cm}^{-1}$  is attributed to the  $\nu_{\text{C}=\text{O}}$  bending frequency from amide VI. In general, these assignments for the FT-IR spectra provide strong evi-

dence for chemical bond formation between RGD and GEMcnZIF-8. Further support for surface functionalization of GEMcnZIF-8 with RGD was provided by size exclusion chromatography of acid-digested samples (see ESI, Fig. S3<sup>†</sup>). As expected, no RGD peak was observed in the chromatographic profiles of nZIF-8 or GEMcnZIF-8 whereas RGD peaks were found at the same retention volume in the chromatographic profiles of both pristine RGD and GEMcRGD@nZIF-8. Following these experiments, imaging techniques were utilized to gain further insight into the size, morphology, and surface structure of the nanoparticles.

Accordingly, high-resolution transmission electron microscopy (HR-TEM) images revealed that all particle sizes were within the nanoscale size regime (Fig. 3). This is an important finding, given that particles on the nanoscale are needed for promoting uptake and cytotoxicity within cancer cells.<sup>48</sup> In fact, when compared to particles on the microscale, the smaller-sized nanoparticles can reduce phagocytosis by alveolar macrophages and thereby increase their retention rate within epithelial cells.<sup>49,50</sup> The average size of the non-surface functionalized nZIF-8 and GEMcnZIF-8 were found to be  $76.7$  and  $70.6\text{ nm}$ , respectively. The different sizes and uniformities of nZIF-8 could be explained by coalescence during the nanoparticle growth process. According to the nucleation and growth theory of nanoparticles, the seed formation time is an essential factor in determining the nanoparticle size. As the seeds rapidly developed within a short period of time, the size of the nanoparticle decreases, and the size distribution narrows. This is followed by a coalescence metastable state, in which smaller particles come together before reaching a final formation.<sup>51</sup> Upon surface functionalization to form GEMcRGD@nZIF-8, the average particle size increased by nearly 30% to  $97.9\text{ nm}$ . RGD on the surface of nZIF-8 not only contributed to the difference in size of the overall nano-

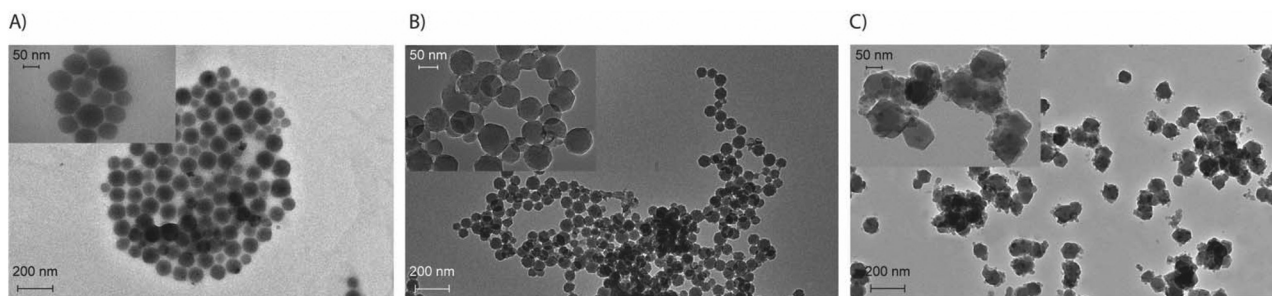


**Fig. 3** Transmission electron microscope images of (A) nZIF-8, (B) GEMCnZIF-8, and (C) GEMCRGD@nZIF-8 with scale bar = 200 nm. Each image provided as an inset is set with a scale bar = 50 nm.

particles, but also to the surface character as the nanoparticle edges of nZIF-8 and GEMCnZIF-8 were noticeably smoother. Additionally, utilizing the same imaging technique, we also studied the stability of parent nZIF-8 in simulated lung fluid (SLF) at pH 7.4 and 6.0, which provides a realistic representation of a lung cancer environment.<sup>52</sup> Following 24 h incubation, the morphology of the nZIF-8 particles in pH 7.4 were found to remain consistent. However, the morphology of the nZIF-8 particles in SLF pH 6.0 were found to be disrupted (see ESI, Fig. S4†), which is a result of the nZIF-8 itself being more responsive in an acidic environment in comparison to a neutral one.<sup>53</sup>

To investigate the surface character even further, atomic force microscopy measurements were performed (see ESI, Fig. S5†). Two- and three-dimensional images showed clear differences in the surface characters of nZIF-8, GEMCnZIF-8, and GEMCRGD@nZIF-8. To assess these differences, a quantitative parameter for the average roughness of each surface,  $R_a$ , was employed. The  $R_a$  value provides a measurement of the peaks and valleys found on sample surfaces. For nZIF-8 and GEMCnZIF-8, smaller peaks and valleys were observed resulting in  $R_a$  values of 12.8 and 12.9 nm, respectively. A pattern of moderate peaks and valleys were observed for the surface character of GEMCRGD@nZIF-8 resulting in a higher  $R_a$  value of 14.7 nm. The results of these measurements imply that surface functionalization of nZIF-8 by RGD does, in fact, increase the surface roughness of the nanoparticles, which strongly correlates with the HR-TEM images obtained. Indeed, these observations are important findings as rougher surface character of nanoparticles is typically correlated with a higher potential for influencing inhibition of certain cancer cell types.<sup>54–56</sup>

The average hydrodynamic sizes of nZIF-8 and GEMCnZIF-8 were similar with values of 104.3 and 101.3 nm, respectively (see ESI, Fig. S6†). Upon surface functionalization, the hydrodynamic size increased to 140 nm. It is noted that hydrodynamic size, as measured by dynamic light scattering techniques, typically leads to higher values than those observed in HR-TEM measurements because the hydration layer around the nanoparticles are included within the calculated size.<sup>57</sup> Regardless, the trend in increasing hydrodynamic size correlates with the trend observed for the HR-TEM measurements.

With respect to the surface charge of the nanoparticles, the zeta potential for nZIF-8 was slightly less positive than GEMCnZIF-8 (+8.44 to +9.04, respectively). Interestingly, both nZIF-8 and GEMCnZIF-8 were significantly less positive when compared with GEMCRGD@nZIF-8 (+20.63). This is another important trend to observe as the more positively charged the surface of nanoparticles are, the more likely they are to be taken up by cancer cell membranes and, thereafter, remain within the cell for longer periods of time.<sup>58</sup>

#### *In vitro* cellular studies

With the structural characterization in hand, our attention then turned to assessing the efficiency of cellular uptake as this is a prerequisite for effective chemotherapeutic delivery when using nanoparticles. To determine the cellular uptake efficiency, we replaced the loading of GEM in nZIF-8 with a fluorescent dye, fluorescein (FI), in order to visualize uptake process between non-functionalized and functionalized nZIF-8 in cancerous human adenocarcinoma alveolar epithelial cells (A549). Accordingly, two new nanoparticles were produced, FICnZIF-8 and FICRGD@nZIF-8, following the same synthetic protocols as before. Once synthesized, A549 cells were treated independently with both FICnZIF-8 and FICRGD@nZIF-8 for 2 h.

The intracellular distribution of FICRGD@nZIF-8 in A549 cells was assessed by fluorescence microscope after staining nuclei with Hoechst 33342. The untreated cells are shown in Fig. 4A. As shown in Fig. 4B and C, higher fluorescence intensity was prominently found in A549 after 2 h treatment of FICRGD@nZIF-8 when compared with FICnZIF-8. In Fig. 4C, it is also clear that after 2 h treatment, FICRGD@nZIF-8 aggregates and accumulates on the cell surface, which indicates endothelial cell attachment greatly reducing the exocytosis process.<sup>59</sup> This finding suggests that, RGD functionalized nZIF-8 binds with an endothelial receptor due to the interaction of the integrin-receptor on the membrane surface of A549 cells, thus promoting fast endothelialization and translocation.<sup>60</sup> These results are in accordance to previous studies on other nanomaterials modified with RGD.<sup>61</sup> Given that RGD@nZIF-8 is able to demonstrate strong cellular interaction in A549, we then further studied its role to deliver GEM and

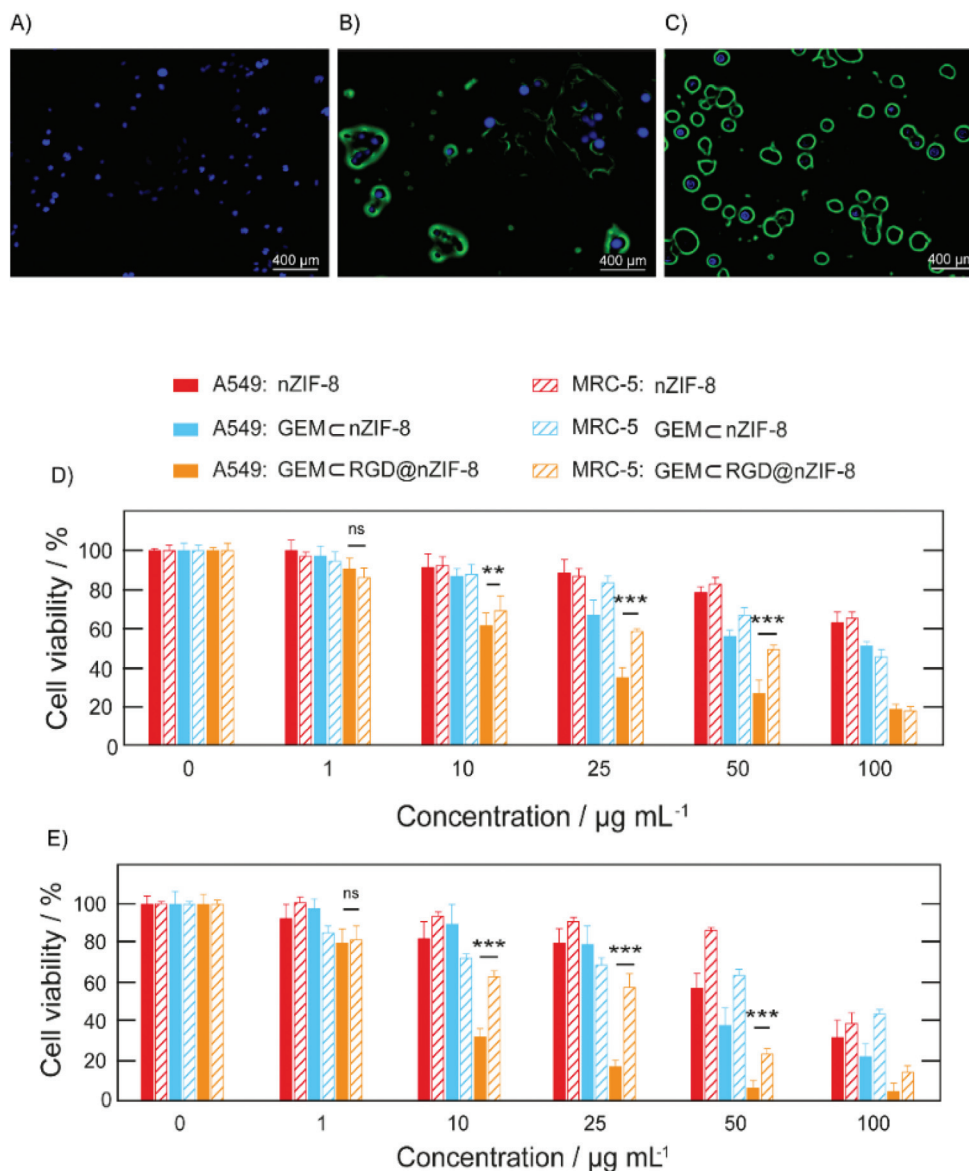


**Fig. 4** Fluorescence microscopy images for (A) untreated, (B) FICnZIF-8, and (C) FICRGD@nZIF-8 comparing the uptake of the functionalize and non-functionalize nZIF-8 nanoparticles within cancerous human lung adenocarcinoma alveolar epithelial cells (A549). Cytotoxicity was evaluated through an MTT assay after treating A549 cells (solid bars) and normal human lung fibroblast (MRC-5) cells (dashed bars) with nZIF-8 (red), GEMcnZIF-8 (blue), and GEMCRGD@nZIF-8 (orange) for (D) 24 and (E) 48 h. Shown are cell viability percentages as a function of concentration of the nanoparticles used in the treatment. Error bars depict standard deviation ( $n = 3$ ). Code: ns = non-significant; \*\*= $P < 0.01$ ; and \*\*\*= $P < 0.001$ .

induce a certain level of cytotoxicity towards cancer cells as compared to normal cells.

As such, A549 and MRC-5 cell lines were incubated with various concentrations of nZIF-8, GEMcnZIF-8, GEMCRGD@nZIF-8 and pristine GEM for 24 and 48 h. The cytotoxicity was then evaluated through a MTT assay with Fig. 4D and E, illustrating the percentage of cell viability after 24 and 48 h of treatment. From these experiments, it is concluded that GEMCRGD@nZIF-8 displays concentration-dependent cytotoxicity toward A549 cells following both 24 and 48 h treatments when compared with nZIF-8 and GEMcnZIF-8. Certain level cytotoxicity was also evident for

GEMCRGD@nZIF-8 toward MRC-5 cells after 24 h of treatment. It is important to point out the reason for this. Given the fact that normal lung fibroblast cells, including MRC-5, have been reported to temporarily express  $\alpha V\beta 3$  integrins on the cell surface, RGD is capable of recognizing the signal emitted from the  $\alpha V\beta 3$  integrins, thereby exhibit certain level of cytotoxicity effect. This is supported by previous reports, in which it was shown that chitosan conjugated RGD formulation exhibited cytotoxicity effects in normal fibroblast cells, but not to normal bronchial epithelial cells with no integrins expression.<sup>62</sup> Next, the concentration of GEMCRGD@nZIF-8 at  $10 \mu\text{g mL}^{-1}$  induced 39 and 31% cell death for the A549 and

MRC-5 lines ( $P < 0.01$ ), respectively, at the 24 h mark. Remarkably after 48 h, the percentage of cell death increased significantly ( $P < 0.001$ ), by GEMcRGD@nZIF-8 for A549 (75%) compared with MRC-5 (37%), indicating better toxicity induc-

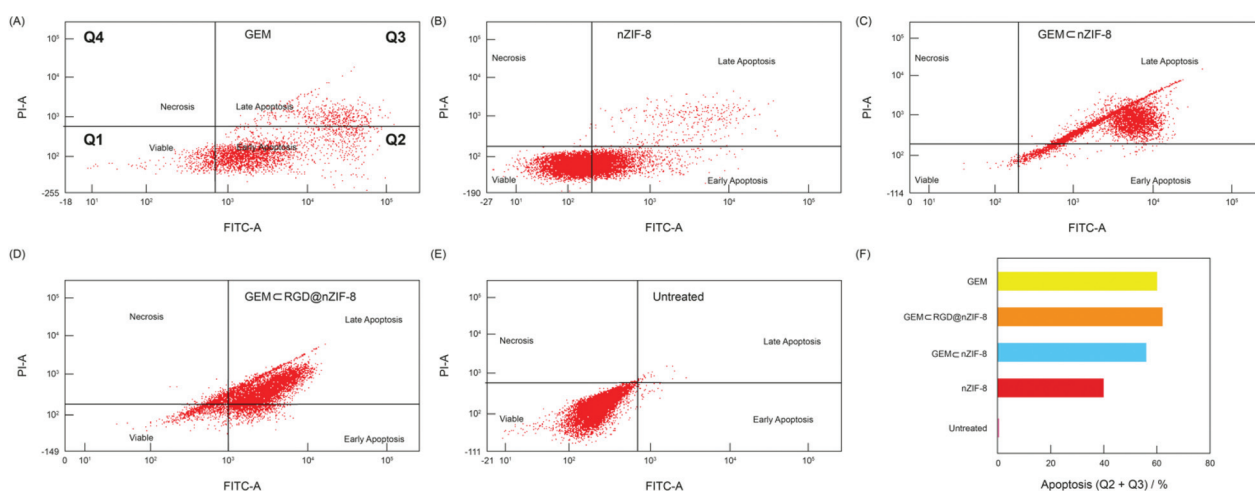
tion toward A549 than MRC-5. At lower concentration ( $1 \mu\text{g mL}^{-1}$ ), it was determined that  $>80\%$  of cells were viable for both A549 and MRC-5 cell lines after treatment with GEMcRGD@nZIF-8 for up to 48 h. This means that at this low

**Table 1**  $\text{IC}_{50}$  values for pristine GEM, nZIF-8, GEMc nZIF-8, and GEMcRGD@nZIF-8 upon treatment of A549 and MRC-5 cells

	Pristine GEM		nZIF-8		GEMc nZIF-8		GEMcRGD@nZIF-8	
	24	48	24	48	24	48	24	48
IC <sub>50</sub> for A549 cells ( $\mu\text{g mL}^{-1}$ )	$1.4 \pm 1.4$	$1.4 \pm 0.2$	$81.5 \pm 2.1$	$50 \pm 6.9$	$52.9 \pm 1.6$	$34.4 \pm 2.9$	$11.2 \pm 0.6$	$5.2 \pm 1.0$
IC <sub>50</sub> for MRC-5 cells ( $\mu\text{g mL}^{-1}$ )	$0.4 \pm 0.1$	$0.3 \pm 0.2$	$98.5 \pm 6.9$	$80.2 \pm 2.0$	$61.7 \pm 1.7$	$42.4 \pm 2.9$	$27 \pm 3.2$	$20.7 \pm 1.0$
Selectivity index (SI) <sup>a</sup>	0.29	0.21	1.21	1.6	1.2	1.23	2.41	3.98

<sup>a</sup> SI =  $\text{IC}_{50}$  (normal lung fibroblast, MRC-5/lung cancer, A549).

#### Human Adenocarcinoma Alveolar Epithelial Cells (A549)



#### Normal Human Lung Fibroblast (MRC-5)

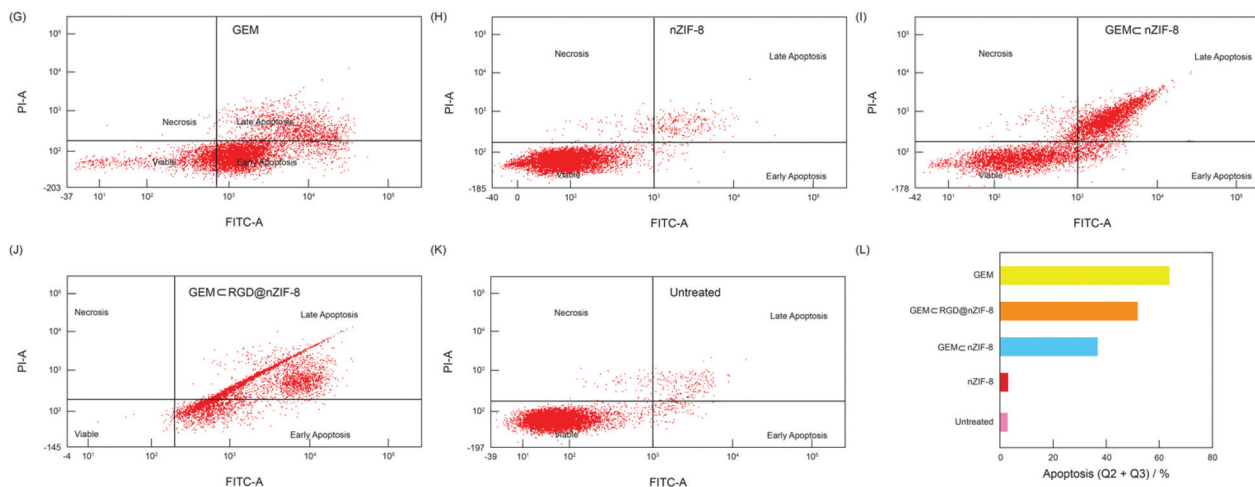


**Fig. 5** Quantification of apoptotic cell population obtained by flow cytometry analysis at 48 h time point. Dot plots of A549 (A–E) and MRC-5 (G–J) after treated with the appropriate  $\text{IC}_{50}$  value (50% inhibiting concentration) of GEM, nZIF-8, GEMc nZIF-8, and GEMcRGD@nZIF-8. The untreated is provided in (E) and (K). Graphical representation of total percentage of apoptotic cells for each is provided in (F) and (L). The cells populations were illustrated as Q1 (annexin V negative/PI negative) indicating viable cells, Q2 (annexin V positive/PI negative indicating early apoptotic cells, Q3 (annexin V positive/PI positive) indicating late apoptotic cells, and Q4 (annexin V negative/PI positive) indicating necrotic cells. The percentage of apoptotic cells were calculated as the sum of Q2 + Q3. A minimum of 10 000 cells were counted and processed using software FACSDiva Version 6.1.3.

concentration, GEMCRGD@nZIF-8 was non-cytotoxic. Following the cell viability data, the 50% cell growth inhibition ( $IC_{50}$ ) values for each treatment were calculated.

Table 1 shows the  $IC_{50}$  and selectivity index (SI) values of nZIF-8, GEMCnZIF-8, GEMCRGD@nZIF-8, and GEM in A549 and MRC-5 cell lines. In general, the  $IC_{50}$  values for all nanoparticles after 24 and 48 h of treatment, were lower for A549 as compared to MRC-5 cells. In the absence of a nanocarrier, pristine GEM exhibited the lowest  $IC_{50}$  value and showed no significant differences ( $P > 0.05$ ) when treating A549 and MRC-5 for 24 and 48 h. The  $IC_{50}$  values for GEMCRGD@nZIF-8 were  $11.2 \pm 0.6$  and  $5.2 \pm 1.0 \mu\text{g mL}^{-1}$  ( $P < 0.001$ ) in A549 cells after 24 and 48 h treatments, respectively, whereas the  $IC_{50}$  values for GEMCnZIF-8 were  $52.9 \pm 1.6$  and  $34.4 \pm 2.9 \mu\text{g mL}^{-1}$ , respectively. These findings indicated the functionalized nanoparticles were significantly better inhibit the 50% cancer cell growth compared to non-functionalized nanoparticles. With respect to MRC-5, the  $IC_{50}$  values for GEMCRGD@nZIF-8 were higher after 24 and 48 h ( $P < 0.001$ ;  $27.0 \pm 3.2$  and  $20.7 \pm 1.0 \mu\text{g mL}^{-1}$ , respectively). These results have shown that the functionalized nanoparticles were significantly better to inhibit the A549 cells compared with MRC-5 cells. Next, we further assessing the selectivity of all nanoparticles and pristine GEM towards cancer cells. The selectivity was indicated by selectivity index (SI) =  $IC_{50}$  normal cell/ $IC_{50}$  cancer cell. When assessing the selectivity, it is important to note that  $SI > 2$  is considered to be significant and selective towards cancer cells.<sup>63</sup> Interestingly, the GEMCRGD@nZIF-8 demonstrated a higher selectivity towards A549 as evidenced by SI values of 2.41 for 24 h and 3.98 for 48 h of treatment, respectively. Larger SI values were observed for longer rather than shorter treatment periods, which were accompanied by smaller  $IC_{50}$  values (Table 1). Meanwhile, pristine GEM, nZIF-8, and GEMCnZIF-8 all produced SI values  $< 2$  for treatments of A549 cells, thereby indicating a lower selectivity towards A549.<sup>64</sup> Based on the significant cytotoxicity induction and selectivity values, the GEMCRGD@nZIF-8 has been demonstrated as a selective and active-targeting behavior of nanoparticles for lung cancer cells.

Given that GEMCRGD@nZIF-8 was found to be selective in enhancing the cytotoxicity of cancer cells, we then sought to quantify the apoptotic cell population further *via* flow cytometry (Fig. 5). In the flow cytometry measurements, both A549 and MRC-5 cell lines were exposed to pristine GEM, nZIF-8, GEMCnZIF-8, and GEMCRGD@nZIF-8 for 48 h. Viable cells are depicted in the lower left quadrant (Q1). Early apoptotic cells, which were positively stained only for Annexin V/FITC, are plotted in the lower right quadrant (Q2). Late apoptotic cells that were stained positive for both Annexin V/FITC and PI are plotted in the upper right quadrant (Q3). The PI-only stained necrotic cells are displayed in the upper left quadrant (Q4).

When exposed to nZIF-8, GEMCnZIF-8, and GEMCRGD@nZIF-8, the total percentage of apoptotic cells (Q2 + Q3) in A549 were observed to be higher than MRC-5. Furthermore, the total apoptotic cells observed after treatment

with pristine GEM alone was found to be comparable in both A549 and MRC-5 cell lines. Notably, the treatment of A549 cells by GEMCRGD@nZIF-8, yielded enhanced apoptotic cells (62%) in comparison to the GEMCnZIF-8 (55.9%) and pristine GEM alone (60%). The GEMCRGD@nZIF-8 also showed a lower number of apoptotic cells (51.6%) in MRC-5 in comparison with treatment by pristine GEM alone (63.5%). These findings reveal that functionalized GEMCRGD@nZIF-8 is capable of inducing apoptosis in A549 while reducing cell death in MRC-5 cells. Once again, we attribute this to the fact that the RGD homing peptides are more likely to actively-bind the over-expression of  $\alpha V\beta 3$  integrins on the outer surface of A549 cells.<sup>65</sup> Finally, we note that a follow-up study is being planned to perform deeper investigations into apoptotic populations that are induced by the synergistic reaction of RGD@ZIF-8 at its  $IC_{50}$  value.

## Conclusion

Through a straightforward, one-pot solvothermal synthetic approach, we have reported the loading and subsequent functionalization of nZIF-8 with an anti-cancer agent (GEM) and an autonomous homing system (RGD peptide), respectively. After full structural physicochemical characterization, the resulting nanoparticle, RGD@nZIF-8, demonstrated enhanced cellular uptake within cancerous human adenocarcinoma alveolar epithelial cells (A549). Following this, the GEM-loaded analogue of this functionalize nanoparticle, GEMCRGD@nZIF-8, exhibited a smaller  $IC_{50}$  value with significantly more selectivity toward cancer cells (A549) than normal cells (MRC-5). The apoptotic population in A549 cells was also observed to increase after treatment by GEMCRGD@nZIF-8. In summary, this work presents a new strategy for realizing a nano-sized zeolitic imidazolate framework that actively targets cancer cells *via* an autonomous homing peptide system on its surface in order to effectively deliver chemotherapeutic payload.

## Experimental

### Materials and supplies

Zinc nitrate hexahydrate ( $Zn(NO_3)_2 \cdot 6H_2O$ ; 99% purity), 2-methylimidazole (99% purity), gemcitabine (99% purity), fluorescein (95% purity), *p*-formaldehyde (95% purity), 3-[4,5-dimethylthiazol-2-yl]-2,5-diphenyltetrazolium bromide (MTT; 98% purity) and dimethyl sulfoxide (DMSO; 99.5% purity) were purchased from Sigma Aldrich. Methanol ( $\geq 99.9\%$  purity), acetonitrile ( $\geq 99.9\%$  purity) and triethylamine (99.5% purity) were acquired from Fisher Scientific. Arg-Gly-Asp (RGD) homing peptide was purchased from GL Biochem. Cancerous human lung adenocarcinoma alveolar epithelial cells (A549) and normal human lung fibroblast cells (MRC-5) were purchased from American Type Culture Collection (ATCC). RPMI-1640, fetal bovine serum (FBS), trypsin-EDTA and anti-



biotic-antimycotic solution were purchased from Nacalai Tesque. Phosphate buffer saline (PBS) were obtained from Gibco. Hoechst 33342 was received from Invitrogen. Annexin V-FITC/propidium iodide (PI) dual kit were procured from Sangon Biotech. Ultra-pure water was generated using a Milli-Q gradient water system. All chemicals were used as received without further purification.

### Structure characterization

High-performance liquid chromatography (HPLC; Waters Corporation, Milford, Massachusetts, USA) analyses were performed with a C<sub>18</sub> column (Phenomenex C<sub>18</sub> column: 3.5  $\mu$ m, 4.6  $\times$  150 mm). Size exclusion-chromatography (SEC) was performed on an Akta Avant system. Crystallinity and structural identification of all materials presented in this work was assessed by powder X-ray diffraction analysis (PXRD) on a PANalytical X'Pert Pro-MPD diffractometer equipped with an image plate detector using Cu K $\alpha$  radiation ( $\lambda = 1.540598 \text{ \AA}$ ) in continuous scan mode. For each PXRD measurement, samples were prepared at room temperature (25  $^{\circ}$ C) by placing the dry powder onto a sample holder and flattening the crystals with a spatula. Fourier transform infrared (FT-IR) spectra were collected using a Nicolet 6700 FT-IR-attenuated total reflection (FT-IR-ATR) spectrophotometer over a range of 4000 to 400  $\text{cm}^{-1}$ . The output FT-IR absorption bands are described as follows: vs, very strong; s, strong; m, medium; sh, shoulder; w, weak; vw, very weak; br, broad. Particle size and structural morphology were identified using a field emission JEOL 2010F high-resolution transmission electron microscope (HR-TEM) operated at 200 kV. For all HR-TEM measurements, samples were prepared by diluting 30  $\mu$ L of a dispersed sample to 300  $\mu$ L using methanol, at which point, 5  $\mu$ L of the diluted, dispersed sample was drop-casted onto a carbon-coated copper TEM grid. Once drop-casted, the methanol solvent was allowed to evaporate under a heat lamp. Surface imaging was analyzed using a Bruker Dimension EDGE atomic force microscope (AFM) in tapping mode at a scanning rate of 0.9 Hz. For this measurement, samples were suspended in methanol, transferred to a glass slide, and air dried at room temperature. Low-pressure N<sub>2</sub> adsorption isotherms were recorded on a Micromeritics Tristar II. A liquid-N<sub>2</sub> bath was used for measurements at 77 K. All samples were degassed at 120  $^{\circ}$ C for 8 h prior to recording the adsorption isotherm. Surface charge and hydrodynamic size were measured using a Zetasizer Nano ZS Malvern dynamic light scattering (DLS) instrument. Prior to performing the DLS experiments, all samples were diluted 8-fold with respect to the initial concentration using methanol. Finally, thermal gravimetric analysis (TGA) was measured on a PerkinElmer STA6000 thermal analysis system with the sample held in an alumina pan heated from 50 to 800  $^{\circ}$ C (rate of 10  $^{\circ}$ C  $\text{min}^{-1}$ ) under continuous N<sub>2</sub> flow.

### Cell analysis equipment

Fluorescence imaging for cellular uptake was carried out with a Carl Zeiss fluorescence microscope. The images were taken

with a Zeiss AxioCam MRm camera and processed with Zen Lite 2012 software. The absorbance of formazan crystals was measured using a Biotek Instrument enzyme-linked immunoassay (ELISA) microplate reader. Finally, the apoptotic cells population were quantified by a BD LSRFortessa flow cytometer and the plots were analyzed using BD FACSDiva 6.1.3.

### Synthesis of nano-ZIF-8 (nZIF-8)

The synthesis of nano-ZIF-8 (nZIF-8) was carried out with slight modifications to a previously reported recipe.<sup>66</sup> In a typical synthesis, Zn(NO<sub>3</sub>)<sub>2</sub>·6H<sub>2</sub>O (0.3 g, 1.01 mmol) and 2-methylimidazole (0.66 g, 8.04 mmol) were weighed separately and each dissolved in 14.3 mL methanol. Once dissolved, the 2-methylimidazole solution was added to the Zn(NO<sub>3</sub>)<sub>2</sub>·6H<sub>2</sub>O solution and the resulting reaction mixture was slowly stirred at 100 rpm with a magnetic stir bar. After 15 min, the milky mixture was centrifuged at 4025g for 10 min, at which point the precipitate was collected and washed with methanol (10 mL). This washing process was repeated three times before drying the collected solid in an open-air oven at 80  $^{\circ}$ C for 12 h. FT-IR (4000–400  $\text{cm}^{-1}$ ): 1577  $\text{cm}^{-1}$  (vw), 1300–1450  $\text{cm}^{-1}$  (sh), 1142  $\text{cm}^{-1}$  (m), 992  $\text{cm}^{-1}$  (m), 691  $\text{cm}^{-1}$  (w), and 420  $\text{cm}^{-1}$  (s).

### Stability of nanoZIF-8 (nZIF-8) in simulated lung fluid (SLF)

The nZIF-8 were incubated in simulated lung fluid (SLF) having pH 7.5 and 6.0 at room temperature. After 24 h of incubation, the nZIF-8 was placed in different pH SLF suspensions. The nanoparticles were then processed following similar procedures as described above for HR-TEM analysis.

### Encapsulation of gemcitabine (GEM) within nZIF-8 (GEMCnZIF-8)

Zn(NO<sub>3</sub>)<sub>2</sub>·6H<sub>2</sub>O (0.3 g, 1.01 mmol) and 2-methylimidazole (0.66 g, 8.04 mmol) were weighed separately and each dissolved in 14.3 mL methanol. After dissolving, a solution of gemcitabine (GEM; 8 mg in 1 mL methanol) was added to the Zn(NO<sub>3</sub>)<sub>2</sub>·6H<sub>2</sub>O solution and the resulting reaction mixture was stirred for 5 min at 500 rpm with a magnetic stir bar at room temperature. Next, the 2-methylimidazole solution was added to the Zn(NO<sub>3</sub>)<sub>2</sub>·6H<sub>2</sub>O and GEM reaction mixture and continuously stirred at 500 rpm with a magnetic stir bar at room temperature. After 15 min of stirring, the milky suspension was centrifuged at 4025g for 10 min, at which point the supernatant was decanted and the remaining solid product was washed with 10 mL of methanol three times and then air-dried at room temperature for 12 h. FT-IR (4000–400  $\text{cm}^{-1}$ ): 1577  $\text{cm}^{-1}$  (vw), 1300–1450  $\text{cm}^{-1}$  (sh), 1142  $\text{cm}^{-1}$  (m), 992  $\text{cm}^{-1}$  (m), 691  $\text{cm}^{-1}$  (w) and 420  $\text{cm}^{-1}$  (s).

### Surface functionalization of GEMCnZIF-8 using Arg-Gly-Asp (RGD) homing peptide (GEMC RGD@nZIF-8)

Zn(NO<sub>3</sub>)<sub>2</sub>·6H<sub>2</sub>O (0.3 g, 1.01 mmol) and 2-methylimidazole (0.66 g, 8.04 mmol) were weighed separately and each dissolved in 14.3 mL methanol. After dissolving, a solution of gemcitabine (GEM; 8 mg in 1 mL methanol) was added to the

Zn(NO<sub>3</sub>)<sub>2</sub>·6H<sub>2</sub>O solution and the resulting reaction mixture was stirred for 5 min at 500 rpm with a magnetic stir bar at room temperature. Next, the 2-methylimidazole solution was added to the Zn(NO<sub>3</sub>)<sub>2</sub>·6H<sub>2</sub>O and GEM reaction mixture and continuously stirred at 500 rpm with a magnetic stir bar at room temperature. After 15 min, triethylamine (1 mL, 7 mmol) was added to the milky suspension with gentle stirring at 100 rpm for 5 min at room temperature. Next, a solution of the peptide (1 mg peptide in 1 mL methanol), Arg-Gly-Asp (RGD), was added to the mixture with gentle stirring at 100 rpm for 16 h at room temperature. After 16 h, the reaction mixture was then centrifuged at 4025g for 10 min, at which point the supernatant was decanted and the remaining solid product was collected and washed with 10 mL of methanol three times, air-dried at room temperature for 12 h, and stored at 4 °C until further use. FT-IR (4000–400 cm<sup>-1</sup>): 3300–3100 cm<sup>-1</sup> (br), 1736 cm<sup>-1</sup> (m), 1648 cm<sup>-1</sup> (vw), 1577 cm<sup>-1</sup> (w), 1375 cm<sup>-1</sup> (m) and 524 cm<sup>-1</sup> (w).

#### GEM loading amount and encapsulation efficiency within nZIF-8

After the reaction mixture finished stirring for 16 h, an aliquot of the supernatant was obtained for analysis of GEM loading amount and encapsulation efficiency. This analysis was performed using HPLC with an acetonitrile and water mixture (10:90 v/v) as the mobile phase at a flow rate of 1 mL min<sup>-1</sup>. The absorption detector for GEM was set at 268 nm. The GEM loading amount (GL%) and encapsulation efficiency (EE%) within nZIF-8 was calculated as follows: GL% = [amount of GEM in nZIF-8/weight (mg) of nZIF-8] × 100 and EE% = [amount of GEM in nZIF-8/amount of GEM added to the encapsulation process] × 100.

#### RGD identification profile

After the surface of GEMCnZIF-8 was functionalized with RGD, the extracted solid product was digested in 50 µL of 2 M hydrochloric acid. The digested solution was analyzed *via* SEC at room temperature using 20% methanol to water at a flow rate of 0.5 mL min<sup>-1</sup>. The presence of RGD was assessed by comparing the peak profile inferred from pristine RGD with that of RGD@nZIF-8.

#### Encapsulation of fluorescein (FI) within nZIF-8 and RGD@nZIF-8 (FICnZIF-8 and FICRGD@nZIF-8, respectively)

The encapsulation of fluorescein within nZIF-8 and RGD@nZIF-8 followed the same procedures as described above by simply replacing GEM with fluorescein in the recipe.

#### *In vitro* cellular studies

Cancerous human adenocarcinoma alveolar epithelial (A549) and normal human lung fibroblast (MRC-5) cell lines were cultured in RPMI-1640 enriched with 10% fetal bovine serum (FBS, v/v), and 1% antibiotic-antimycotic solution (v/v). Both cell lines were maintained at 37 °C under a humidified atmosphere that contained 5% CO<sub>2</sub>. Following confluence, the cells

were sub-cultured into a new media and cellular studies were then conducted.

#### Cellular uptake

A549 cells were seeded at a density of  $2 \times 10^5$  cells per well in a 6-well plate and allowed to adhere for 24 h. The cells were treated with FICnZIF-8 and FICRGD@nZIF-8 as a model drug in equivalent concentration (10 µg mL<sup>-1</sup>) for 2 h. After treatment, the cells were then washed with phosphate buffered saline solution (PBS) and fixed in 4% *p*-formaldehyde. The untreated cells were assigned as control. This was followed by nuclear DNA staining with Hoechst 33342 (blue) prior to examination *via* fluorescence microscopy. For fluorescence detection, 450 and 517 nm bandpass filters were used for blue and green fluorescence, respectively.

#### Cytotoxicity assay

The MTT assay was performed to evaluate potential cytotoxicity of GEM, nZIF-8, GEMCnZIF-8, GEMCRGD@nZIF-8. For this study, A549 ( $4 \times 10^3$  cells per well) and MRC-5 ( $5 \times 10^3$  cells per well) were seeded and allowed to adhere for 24 and 48 h. The respective cells were then treated with pristine GEM, nZIF-8, GEMCnZIF-8, GEMCRGD@nZIF-8 for 24 and 48 h. The concentration ranged from 0–100 µg mL<sup>-1</sup>. After treatment, 20 µL of MTT solution (5 mg mL<sup>-1</sup> in PBS) was then added to each well and left to incubate for 3 h. Subsequently, 80 µL DMSO was added to each well to solubilize the formazan crystals. The absorbance (Abs) at 570 nm was measured with an enzyme-linked immunoassay (ELISA) microplate reader. The percentage of cell viability was calculated as follows:<sup>67</sup> Cell viability (%) = [Abs<sub>treated cells</sub>/Abs<sub>untreated cells</sub>] × 100. Following the calculation and analysis of cell viability, the 50% cell growth inhibition (IC<sub>50</sub>) values for each tested sample were calculated using curve-fitting methods with statistical analysis software for both A549 and MRC-5. Using the IC<sub>50</sub> values of A549 and MRC-5, the selectivity indices (SI) towards cancer cells for each tested nanoparticles and pristine GEM were calculated as follows:<sup>68</sup>

$$SI = [IC_{50}(\text{normal cell})/IC_{50}(\text{cancer cell})].$$

#### Cellular apoptosis

A549 and MRC-5 cells were seeded at a density of  $2 \times 10^5$  cells per well in a 6-well plate and allowed to adhere for 24 h. The cells were then treated with GEM, nZIF-8, GEMCnZIF-8, and GEMCRGD@nZIF-8 at their IC<sub>50</sub> value for 48 h. After treatment, cells were trypsinized and washed with PBS, at which point 100 µL of 1× binding buffer was added. Subsequently, 5 µL of Annexin V-FITC and 2 µL propidium iodide were added to the cell-containing 1× buffer. The cell mixtures were then incubated for 15 min at 25 °C. After this time elapsed, 1× buffer (400 µL) was added prior to flow cytometric analysis. For each sample, a minimum of 10 000 cells were counted. The percentage of apoptosis were calculated as the sum of Q2 + Q.<sup>69</sup>

## Statistical analysis

All statistical analyses in the experiments described above were analyzed using Graph Pad Prism 8.0. The error bars represent the mean values with standard deviation (SD) unless otherwise indicated. The statistical significance level was set at 0.05.

## Author contributions

Nurul Akmarina Mohd Abdul Kamal: formal analysis, methodology, investigation, data curation, writing-original draft, review & editing. Emilia Abd Malek: data curation, supervision, funding acquisition, writing – review & editing. Sharida Fakurazi: data curation, supervision, writing – review & editing. Kyle. E. Cordova: formal analysis, data curation, writing – review & editing. Mohd Basyaruddin Abdul Rahman: conceptualization, supervision, funding acquisition, writing – review & editing.

## Conflicts of interest

All authors declare no competing interests.

## Acknowledgements

We are grateful to Ministry of Higher Education, Malaysia under LRGS NanoMITe (Grant RU029-2014, No. 5526306) and Universiti Putra Malaysia for providing financial support for this work (Grant GP-IPB/2017, No. 9580901). We thank Prof. Omar M. Yaghi (University of California, Berkeley) for his support of global science activities.

## References

- 1 F. Bray, J. Ferlay, I. Soerjomataram, R. L. Siegel, L. A. Torre and A. Jemal, *Cancer J. Clin.*, 2018, **68**, 394–424.
- 2 C. C. S. Dela, L. T. Tanoue and R. A. Matthay, *Clin. Chest Med.*, 2011, **32**, 605–644.
- 3 C. Manegold, *Expert Rev. Anticancer Ther.*, 2004, **4**, 345–360.
- 4 J. Ciccolini, C. Serdjebi, G. J. Peters and E. Giovannetti, *Cancer Chemother. Pharmacol.*, 2016, **78**, 1–12.
- 5 C. Zappa and S. A. Mousa, *Transl. Lung Cancer Res.*, 2016, **5**, 288–300.
- 6 B. Hryciuk, B. Szymanowski, A. Romanowska, E. Salt, B. Wasąg, B. Grala, J. Jassem and R. Duchnowska, *Oncol. Lett.*, 2018, **15**, 1912–1916.
- 7 S. K. Golombek, J. May, B. Theek, L. Appold, N. Drude, F. Kiessling and T. Lammers, *Adv. Drug Delivery Rev.*, 2018, 17–38.
- 8 X. J. Lee, H. N. Lim, N. S. K. Gowthaman, M. B. A. Rahman, C. A. C. Abdullah and K. Muthoosamy, *Appl. Surf. Sci.*, 2020, **512**, 145738.
- 9 N. A. Wahgiman, N. Salim, M. B. A. Rahman and S. E. Ashari, *Int. J. Nanomed.*, 2019, **14**, 7323–7338.
- 10 C. F. Cheok, *Cell Cycle*, 2012, **11**, 2227.
- 11 S. E. Harrington and T. J. Smith, *J. Am. Med. Assoc.*, 2008, **299**, 2667–2678.
- 12 Y. Barenholz, *J. Controlled Release*, 2012, **160**, 117–134.
- 13 A. P. Singh, A. Biswas, A. Shukla and P. Maiti, *Signal Transduction Targeted Ther.*, 2019, **4**, 1–21.
- 14 P. Grodzinski, M. Kircher, M. Goldberg and A. Gabizon, *ACS Nano*, 2019, **13**, 7370–7376.
- 15 H. He, L. Liu, E. E. Morin, M. Liu and A. Schwendeman, *Acc. Chem. Res.*, 2019, **52**, 2673–2683.
- 16 A. Gothwal, I. Khan and U. Gupta, *Pharm. Res.*, 2016, **33**, 18–39.
- 17 Z. J. Chen, S. C. Yang, X. L. Liu, Y. Gao, X. Dong, X. Lai, M. H. Zhu, H. Y. Feng, X. Di Zhu, Q. Lu, M. Zhao, H. Z. Chen, J. F. Lovell and C. Fang, *Nano Lett.*, 2020, **20**, 4177–4187.
- 18 S. Naderinezhad, G. Amoabediny and F. Haghirsadat, *RSC Adv.*, 2017, **7**, 30008–30019.
- 19 A. A. Asmawi, N. Salim, C. L. Ngan, H. Ahmad, E. Abdulmalek, M. J. Masarudin and M. B. Abdul Rahman, *Drug Delivery Transl. Res.*, 2019, **9**, 543–544.
- 20 R. J. Browning, P. J. T. Reardon, M. Parhizkar, R. B. Pedley, M. Edirisinghe, J. C. Knowles and E. Stride, *ACS Nano*, 2017, **11**, 8560–8578.
- 21 H. Li, H. Jin, W. Wan, C. Wu and L. Wei, *Nanomedicine*, 2018, **13**, 1639–1656.
- 22 J. Shi, P. W. Kantoff, R. Wooster and O. C. Farokhzad, *Nat. Rev. Cancer*, 2017, **17**, 20–37.
- 23 P. N. Navya, A. Kaphle, S. P. Srinivas, S. K. Bhargava, V. M. Rotello and H. K. Daima, *Nano Convergence*, 2019, **6**, 23.
- 24 E. M. Pridgen, F. Alexis, T. T. Kuo, E. Levy-Nissenbaum, R. Karnik, R. S. Blumberg, R. Langer and O. C. Farokhzad, *Sci. Transl. Med.*, 2013, **5**, 1–22.
- 25 M. F. Attia, N. Anton, J. Wallyn, Z. Omran and T. F. Vandamme, *J. Pharm. Pharmacol.*, 2019, **71**, 1185–1198.
- 26 N. Muhamad, T. Plengsuriyakarn and K. Na-Bangchang, *Int. J. Nanomed.*, 2018, **13**, 3921–3935.
- 27 T. Simon-Yarza, S. Rojas, P. Horcajada and C. Serre, *Compr. Biomater. II*, 2017, 719–749.
- 28 R. C. Huxford, J. D. Rocca and W. Lin, *Curr. Opin. Chem. Biol.*, 2010, **14**, 262–268.
- 29 H. Zheng, Y. Zhang, L. Liu, W. Wan, P. Guo, A. M. Nyström and X. Zou, *J. Am. Chem. Soc.*, 2016, **138**, 962–968.
- 30 K. Dong, Y. Zhang, L. Zhang, Z. Wang, J. Ren and X. Qu, *Talanta*, 2019, **194**, 703–708.
- 31 Y. Lin, Y. Zhong, Y. Chen, L. Li, G. Chen, J. Zhang, P. Li, C. Zhou, Y. Sun, Y. Ma, Z. Xie and Q. Liao, *Mol. Pharm.*, 2020, **17**, 3328–3341.
- 32 C. Zheng, Y. Wang, S. Z. F. Phua, W. Q. Lim and Y. Zhao, *ACS Biomater. Sci. Eng.*, 2017, **3**, 2223–2229.
- 33 C. Adhikari, A. Das and A. Chakraborty, *Mol. Pharm.*, 2015, **12**, 3158–3166.
- 34 X. Wang, X. Z. Chen, C. C. J. Alcântara, S. Sevim, M. Hoop, A. Terzopoulou, C. de Marco, C. Hu, A. J. de Mello,

- P. Falcaro, S. Furukawa, B. J. Nelson, J. Puigmartí-Luis and S. Pané, *Adv. Mater.*, 2019, **1901592**, 2–8.
- 35 C. Gropp, S. Canossa, S. Wuttke, F. Gándara, Q. Li, L. Gagliardi and O. M. Yaghi, *ACS Cent. Sci.*, 2020, **6**, 1255–1273.
- 36 K. E. Cordova and O. M. Yaghi, *Dalton Trans.*, 2017, **47**, 7634–7639.
- 37 H. Furukawa, K. E. Cordova, M. O’Keeffe and O. M. Yaghi, *Science*, 2013, **341**, 1–12.
- 38 A. Maleki, M. A. Shahbazi, V. Alinezhad and H. A. Santos, *Adv. Healthcare Mater.*, 2020, **9**, 1–42.
- 39 F. Danhier, A. Le Breton and V. Préat, *Mol. Pharm.*, 2012, **9**, 2961–2973.
- 40 S. Ding, G. Chen, W. Zhang, C. Xing, X. Xu, H. Xie, A. Lu, K. Chen, H. Guo, Z. Ren, S. Zheng and L. Zhou, *J. Transl. Med.*, 2015, **13**, 1–13.
- 41 L. Damjanovich, S. M. Albelda, S. A. Mette and C. A. Buck, *Am. J. Respir. Cell Mol. Biol.*, 1992, **6**, 197–206.
- 42 D. Bianconi, M. Unselde and G. W. Prager, *Int. J. Mol. Sci.*, 2016, **17**, 2037.
- 43 L. Yan, X. Chen, Z. Wang, X. Zhang, X. Zhu, M. Zhou, W. Chen, L. Huang, V. A. L. Roy, P. K. N. Yu, G. Zhu and W. Zhang, *ACS Appl. Mater. Interfaces*, 2017, **9**, 32990–33000.
- 44 A. Tiwari, A. Singh, N. Garg and J. K. Randhawa, *Sci. Rep.*, 2017, **7**, 1–12.
- 45 Y. Zhang, Y. Jia, M. Li and L. Hou, *Sci. Rep.*, 2018, **8**, 1–7.
- 46 A. Tiwari, A. Singh, N. Garg and J. K. Randhawa, *Sci. Rep.*, 2017, **7**, 1–12.
- 47 R. Röder, T. Preiß, P. Hirschle, B. Steinborn, A. Zimpel, M. Höhn, J. O. Rädler, T. Bein, E. Wagner, S. Wuttke and U. Lächelt, *J. Am. Chem. Soc.*, 2017, **139**, 2359–2368.
- 48 P. Foroozandeh and A. A. Aziz, *Nanoscale Res. Lett.*, 2018, **6**, 1–12.
- 49 G. Oberdörster, E. Oberdörster and J. Oberdörster, *Environ. Health Perspect.*, 2005, **113**, 823–839.
- 50 S. Ahmad, D. O. Raemy, J. E. Loader, J. M. Kailey, K. B. Neeves, C. W. White, A. Ahmad, P. Gehr and B. M. Rothen-Rutishauser, *J. Aerosol Med. Pulm. Drug Delivery*, 2012, **25**, 7–15.
- 51 N. T. K. Thanh, N. Maclean and S. Mahiddine, *Chem. Rev.*, 2014, **114**, 7610–7630.
- 52 J. Pang, H. Xing, Y. Sun, S. Feng and S. Wang, *Biomed. Pharmacother.*, 2020, **125**, 109861.
- 53 C. Y. Sun, C. Qin, X. L. Wang, G. S. Yang, K. Z. Shao, Y. Q. Lan, Z. M. Su, P. Huang, C. G. Wang and E. B. Wang, *Dalton Trans.*, 2012, **41**, 6906–6909.
- 54 T. Muthukumar, S. Prabhavathi, M. Chamundeeswari and T. P. Sastry, *Mater. Sci. Eng., C*, 2014, **36**, 14–19.
- 55 H. Hashemzadeh, A. Allahverdi, M. Sedghi and Z. Vaezi, *Nanomaterials*, 2020, **10**, 668.
- 56 S. Lee, Y. Lei, D. Wang, C. Li, J. Cheng, J. Wang, W. Meng and M. Liu, *Polymers*, 2019, **11**, 1986.
- 57 P. Eaton, P. Quaresma, C. Soares, C. Neves, M. P. de Almeida, E. Pereira and P. West, *Ultramicroscopy*, 2017, **182**, 179–190.
- 58 E. Blanco, H. Shen and M. Ferrari, *Nat. Biotechnol.*, 2015, **33**, 941–951.
- 59 E. Article, A. Kapara, V. Brunton, D. Graham and K. Faulds, *Chem. Sci.*, 2020, **11**, 5819–5829.
- 60 R. Zhang, X. Qin, F. Kong, P. Chen and G. Pan, *Drug Delivery*, 2019, **26**, 328–342.
- 61 H.-Y. Mi, J. Xin, J. A. Thomsom and L.-S. Turng, *J. Mater. Chem. B*, 2018, **6**, 3485–3485.
- 62 A. Babu, N. Amreddy, R. Muralidharan, G. Pathuri, H. Gali, A. Chen, Y. D. Zhao, A. Munshi and R. Ramesh, *Sci. Rep.*, 2017, **7**, 1–17.
- 63 V. S. Velozo-Sá, L. R. Pereira, A. P. Lima, F. Mello-Andrade, M. R. M. Rezende, R. M. Goveia, W. C. Pires, M. M. Silva, K. M. Oliveira, A. G. Ferreira, J. Ellena, V. M. Deflon, C. K. Grisolia, A. A. Batista and E. P. Silveira-Lacerda, *Dalton Trans.*, 2019, **48**, 6026–6039.
- 64 R. B. Badisa, S. F. Darling-Reed, P. Joseph, J. S. Cooperwood, L. M. Latinwo and C. B. Goodman, *Anticancer Res.*, 2009, **29**, 2993–2996.
- 65 M. Nieberler, U. Reuning, F. Reichart, J. Notni, H. J. Wester, M. Schwaiger, M. Weinmüller, A. Räder, K. Steiger and H. Kessler, *Cancers*, 2017, **9**, 1–33.
- 66 J. Zhuang, C. H. Kuo, L. Y. Chou, D. Y. Liu, E. Weerapana and C. K. Tsung, *ACS Nano*, 2014, **8**, 2812–2819.
- 67 S. Zheng, X. Wang, Y. H. Weng, X. Jin, J. L. Ji, L. Guo, B. Hu, N. Liu, Q. Cheng, J. Zhang, H. Bai, T. Yang, X. H. Xia, H. Y. Zhang, S. Gao and Y. Huang, *Mol. Ther. – Nucleic Acids*, 2018, **12**, 805–816.
- 68 C. B. Braga, L. A. Kido, E. N. Lima, C. A. Lamas, V. H. A. Cagnon, C. Ornelas and R. A. Pilli, *ACS Biomater. Sci. Eng.*, 2020, **6**, 2929–2942.
- 69 R. Zeng, Y. Chen, S. Zhao and G. H. Cui, *Acta Pharmacol. Sin.*, 2012, **33**, 91–100.